RSC Advances

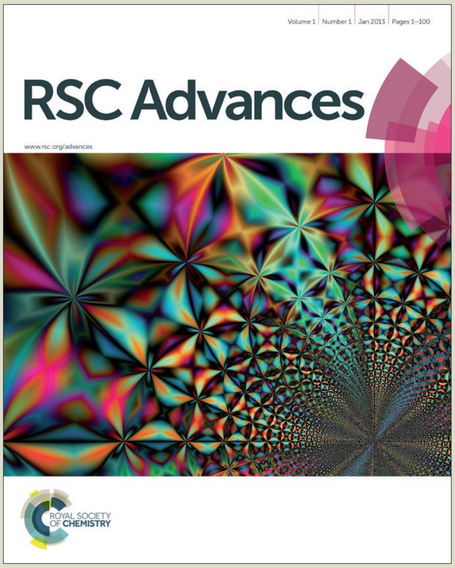

ROYAL SOCIETY OF CHEMISTRY

www.rsc.org/advances

# Hierarchical three-dimensional $NiCo_2O_4$ nanoneedle arrays supported on Ni foam for high-performance supercapacitors

Jian Wu[a,b], Rui Mi[b], Shaomin Li[b], Pan Guo[a], Jun Mei[b], Hao Liu[*,b], Woon-Ming Lau[a,b], Li-Min Liu[*,a]

[a]*Beijing Computational Science Research Center, Beijing 100084, China*
[b]*Chengdu Green Energy and Green Manufacturing Technology R&D Center, Chengdu Development Center of Science and Technology of CAEP, Chengdu, Sichuan, 610207, China*

*Corresponding authors (Hao Liu and Li-Min Liu)

E-mail: mliuhao@gmail.com; Tel.: 0086-28-67076208.

E-mail: limin.liu@csrc.ac.cn; Tel.: 0086-10-82687086.

## Abstract

Three-dimensional (3D) hierarchical $NiCo_2O_4$ nanoneedle arrays have been prepared on nickel foam via a facile hydrothermal method followed by annealing in air. Impressively, when investigated as binder-free supercapacitor electrode, such unique $NiCo_2O_4$ nanoneedle arrays on Ni foam exhibit a superior specific capacitance of 2193 F/g and 1490 F/g at current densities of 1 and 10 A/g calculated based on the active mass of $NiCo_2O_4$, respectively. Furthermore, the areal capacitance is 3.71 F/cm$^2$ at 1 mA/cm$^2$ and 1.39 F/cm$^2$ at 40 mA/cm$^2$. The remarkable electrochemical performance is due to the hierarchical nanoneedle arrays structure with bottom crosslinked nanosheets, which has a large surface area, thus providing more sites to facilitate electrochemical reactions, rapid ion/electron transport, and enhanced strain accommodation. Our results demonstrate that the hierarchical $NiCo_2O_4$ nanoneedle arrays are a promising material as a binder-free electrode for high performance supercapacitors.

# Introduction

Nowadays, the intense concerns over environmental pollution and the limited availability of fossil fuels have led to an ongoing search for clean and renewable energy. Among various energy storage systems, such as fuel cell,[1, 2] capacitors[3-5] and batteries,[6, 7] supercapacitors have attracted intense attention for their high power density, longer cycle lifetime and fast charging-discharging rates. Based on the underlying energy storage mechanism, supercapacitors can be classified into electrical double-layer capacitors (EDLCs) and pseudocapacitors. Furthermore, pseudocapacitors possess a higher specific capacitance, taking advantage of reversible faradaic reactions at the electrode surface. [8-10]

Transition metal oxides (TMOs) and conducting polymers are two main pseudocapacitors materials and have been explored as advanced electrodes for supercapacitors.[11-13] Among these candidates, TMOs are being extensively investigated as high-performance pseudocapacitors due to their rich redox reactions, low cost, low environmental footprint.[14, 15] Unfortunately, their poor intrinsic electrical conductivity hampers their application.[16, 17] Therefore, to fully use the capacitance of TMOs, one must improve their intrinsic electrical conductivity.

Recently, spinel nickel cobaltite ($NiCo_2O_4$) has been suggested to be a promising electrode material for its intriguing advantages including high theoretical capacitance, low cost, environmental friendliness and abundant resources. Particularly, $NiCo_2O_4$ possesses higher electric conductivity and electrochemical activity than those of either nickel oxides or cobalt oxides.[18, 19] Up to now, many methods (hydrothermal,[20] sol-del,[21] electro-deposition,[22] microwave,[23] etc) have been used to prepare $NiCo_2O_4$ with different morphology, such as nanoneedles,[24] nanosheets,[25] nanograss,[26] nanospheres[27] and so forth. Especially, constructing one-dimensional (1D) nanostructures is advantageous in energy storage devices because of efficient ions and electrons transport pathways.[24, 28] In addition, the 1D nanowires structure is not easily pulverized or broken due to its facile strain relaxation, which can be effective against the volume change problem during electrochemical reaction.[29, 30] However, the reported areal capacitance of the 1D structure is usually poor due to low active mass loading. Meanwhile, growing 2D nanosheets on Ni foam have an express path for electron transport and greatly enhance the electrode kinetics due to their open space between sheets.[31, 32] Hence, the ideal electrode architecture should hold the characteristics of high electrical conductivity, facile strain relaxation, fast electron transport and high active mass loading.

In this work, we report a novel approach by cultivating nanoneedle arrays on crosslinked nanosheets grown on Ni foam as binder-free electrodes via a one-step hydrothermal method followed by annealing in air, thus synthesizing 3D hierarchical $NiCo_2O_4$ structures which combine the benefits of 1D and 2D structures. The nanoneedle arrays thus grown exhibit a high specific capacitance of 2193 F/g at current densities of 1 A/g and areal capacitance of 3.71 F/cm$^2$ at 1 mA/cm$^2$. The high capacitance is promising for supercapacitors with high energy and power densities. These remarkable results reveal that such unique hierarchical $NiCo_2O_4$ nanoneedle arrays possess potential applications in electrochemical energy storage.

# Experimental

## Preparation of hierarchical $NiCo_2O_4$ arrays

All chemical reagents in the experiment were of analytical grade and used without further purification. The $NiCo_2O_4$ nanosheet, nanosheet-nanoneedle and nanoneedle arrays were prepared on Ni foam by a one-step hydrothermal synthesis followed by a thermal treatment. Ni foam ($3\times4$ $cm^2$) was carefully cleaned using a diluted HCl solution (2 M) in an ultrasound bath for 20 min to remove the possible surface NiO layer, and then rinsed with deionized (DI) water and ethanol for 10 min each. In a typical procedure, 0.58 g $Co(NO_3)_2\cdot6H_2O$ and 0.29 g $Ni(NO_3)_2\cdot6H_2O$ were dissolved in 40 mL DI water to form a transparent pink solution. 0.08 g of $NH_4F$ and 0.30 g of urea were then added. The solution was transferred into a Teflon-lined stainless steel autoclave of 50 mL. The pretreated Ni foam vertically inserted into the Teflon holder was subsequently soaked in the solution followed by sealing. The autoclave was then heated at 120 ℃ for various reaction times, and cooled to room temperature. The as synthesized sample was rinsed several times with DI water and ethanol, followed by annealing at 350 ℃ in air for 3 h with a slow temperature ramping at a rate of 1 ℃/min to obtain the $NiCo_2O_4$ arrays. The active mass of $NiCo_2O_4$ nanosheets-1h, nanosheets-2h, nanosheets-nanoneedles-4h, and nanoneedles-8h arrays are 0.70, 1.05, 1.33, and 1.64 mg/$cm^2$, respectively.

## Material characterization

The X-ray diffraction (XRD, D/max 2200/PC, Rigaku, 40 kV, 20 mA, Cu $K_\alpha$

radiation, λ = 1.5406 Å) was used to characterize the structure of the product. Scanning electron microscopy (SEM) images and energy dispersive X-ray spectrometer (EDX) were taken with a Hitachi S-5200 scanning electron microscope equipped with energy dispersive X-ray analysis system. Transmission electron microscope (TEM) measurements were carried out by 200 kV side entry JEOL 2010 TEM. Nitrogen adsorption/desorption isotherms were measured at the liquid nitrogen temperature using a Builder SSA-4200 apparatus.

### Electrochemical measurements

All electrochemical experiments were carried out at room temperature using an electrochemical workstation (CHI660D, Shanghai) in a three-electrode cell system. The prepared arrays as the working electrode were investigated with a slice of platinum foil (2 cm × 2 cm) as the auxiliary electrode and Hg/HgO as the reference electrode. The measurements were carried out in two molar potassium hydroxide (KOH) aqueous electrolyte. Cyclic voltammetry (CV) tests were measured in a potential range between 0 and 0.75 V (*vs*. Hg/HgO) at various scan rates, and the charge-discharge processes were performed in the potential window from 0 V to 0.55 V at different current densities. Electrochemical impedance spectroscopy (EIS) measurements were carried out over a wide frequency range of 100 kHz to 0.01 Hz with an AC perturbation of 5 mV. The areal capacitance and specific capacitance (*C*), energy density (*E*) and power density (*P*) can be calculated by the equations: [33, 34]

$$C = \frac{I\Delta t}{S\Delta V} \text{ or } C = \frac{I\Delta t}{m\Delta V} \qquad (1)$$

$$E = \frac{1}{2} C \Delta V^2 \qquad (2)$$

$$P = \frac{E}{\Delta t} \qquad (3)$$

where $I$ (mA) is the discharge current, $S$ (cm$^2$) is the geometrical area of the working electrode. $\Delta V$ (V) and $\Delta t$ (s) represents the potential window and the discharge time, respectively. $m$ is the mass (g) of the active material on the Ni foam.

# Results and discussion

## Structure and Morphology

Hierarchical $NiCo_2O_4$ structures were fabricated on Ni foam through a simple hydrothermal growth together with a post calcination treatment. In the hydrothermal process, the electrochemical reactions are described as follows:[35, 36]

$$\mathrm{Ni^{2+}} + 2\mathrm{Co^{2+}} + 3x\mathrm{F^-} \rightarrow [\mathrm{NiCo_2F_{3x}}]^{3(x-2)-} \qquad (4)$$

$$\mathrm{H_2NCONH_2} + \mathrm{H_2O} \rightarrow 2\mathrm{NH_3} + \mathrm{CO_2} \qquad (5)$$

$$\mathrm{NH_3 \cdot H_2O} \rightarrow \mathrm{NH_4^+} + \mathrm{OH^-} \qquad (6)$$

$$\mathrm{CO_2} + \mathrm{H_2O} \rightarrow \mathrm{CO_3^{2-}} + 2\mathrm{H^+} \qquad (7)$$

$$[\mathrm{NiCo_2F_{3x}}]^{3(x-2)-} + 1.5(2-y)\mathrm{CO_3^{2-}} + 3y\mathrm{OH^-} + n\mathrm{H_2O} \rightarrow$$

$$\mathrm{NiCo_2(OH)_{3y}(CO_3)_{1.5(2-y)}} \cdot n\mathrm{H_2O} + 3x\mathrm{F^-} \qquad (8)$$

The bimetallic (Ni, Co) carbonate hydroxide precursor is transformed to spinel $NiCo_2O_4$ via a facile thermal treatment in air at a relatively low temperature as follows:[35, 36]

$$2\mathrm{NiCo_2(OH)_{3y}(CO_3)_{1.5(2-y)}} \cdot n\mathrm{H_2O} + \mathrm{O_2} \rightarrow$$

$$2\mathrm{NiCo_2O_4} + (3y+2n)\mathrm{H_2O} + 3(2-y)\mathrm{CO_2} \qquad (9)$$

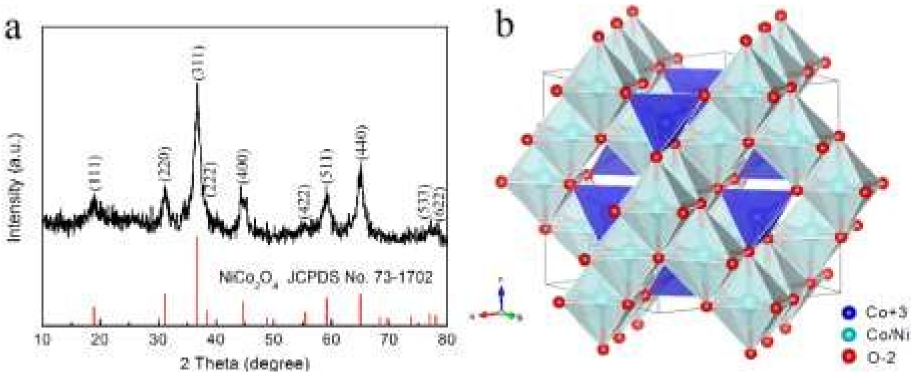

**Fig. 1.** (a) XRD pattern and (b) crystal structure of $NiCo_2O_4$ cubic spinel (ICSD No.02241).

The crystallographic structure of the product is investigated with X-ray diffraction (XRD) as shown in **Fig. S3** and **Fig. 1a**. The Co-Ni bimetallic carbonate hydroxide salts $(NiCo_2(OH)_{3y}(CO_3)_{1.5(2-y)} \cdot nH_2O)$ were formed at the molar ratio of Co/Ni at 2:1, (**Fig. S3**) and decomposed into the $NiCo_2O_4$ in the following annealing process. **Fig. 1a** shows that the identified diffraction peaks of final product can be well indexed to $NiCo_2O_4$ (JCPDS 73-1702). There are no other additional diffraction peaks in the pattern, indicating the high phase purity of $NiCo_2O_4$ formed. **Fig. 1b** shows that $NiCo_2O_4$ adopts a spinel-related structure (space group *Fd*3*m*) with Ni atoms being embedded in the octahedron and Co atoms in both octahedron and tetrahedron.[37, 38] The four apexes of the tetrahedron are shared with octahedron, which form a 3D network of interstitial space for ion diffusion. In addition, the chemical compositions of the products, as analyzed by EDX spectroscopy (**Fig. S4**), indicates the 1:2 atomic ratio of Ni:Co consistent with the stoichiometric ratio of $NiCo_2O_4$.

The porous characteristics of the 3D $NiCo_2O_4$ nanoneedles were investigated by isothermal adsorption and desorption measurements, as shown in **Fig. S5**. The Brunauer-Emmett-Teller (BET) surface area was measured to be 64.01 $m^2/g$. Distinct hysteresis loop appears in the range of 0.7-1.0 $P/P_0$, which reveals the presence of a mesoporous structure of nanoneedles.[35] The inset of **Fig. S5** shows the pore size distribution of the sample calculated by desorption isotherm via Barret-Joyner-Halenda (BJH) method. The as-prepared $NiCo_2O_4$ nanoneedles show narrow distribution of pores at around 7.7 nm. The mesoporous morphological with high surface area characteristics will have impressive electrochemical performance because it is more favorable for electrolyte penetration and fast ion/electron transfer.

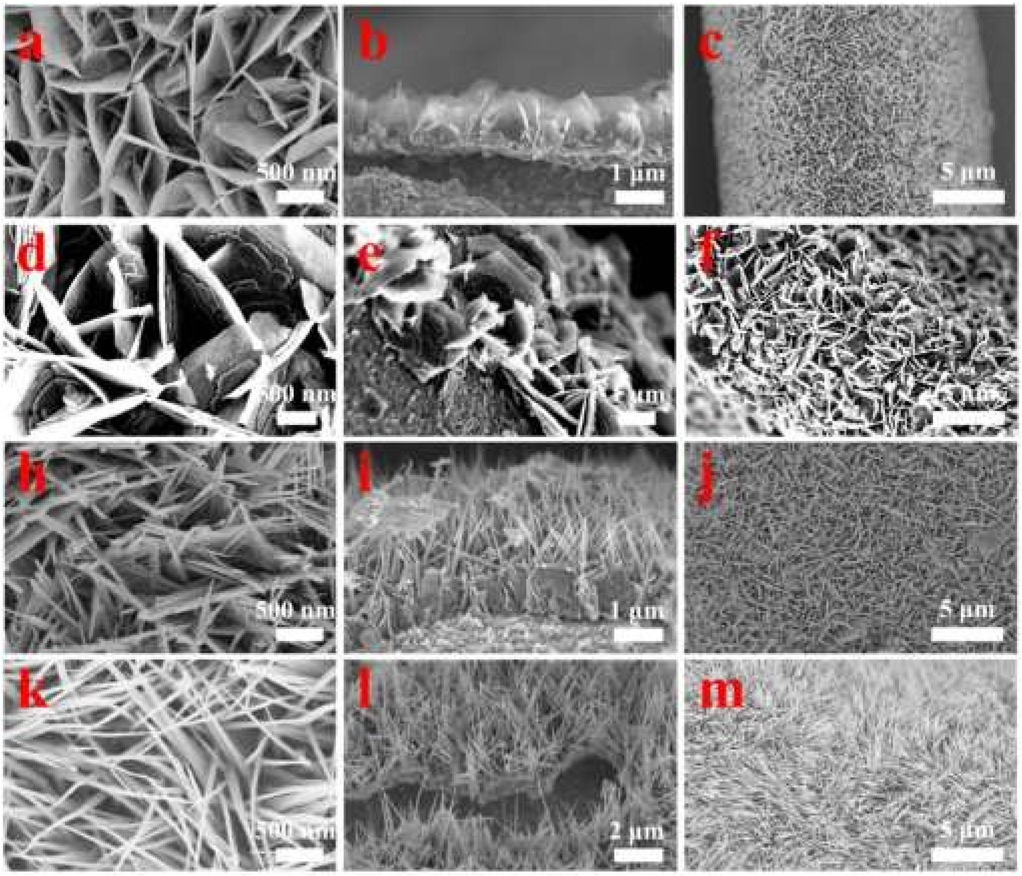

**Fig. 2.** SEM images of the evolution of the hierarchical $NiCo_2O_4$ nanoneedle arrays at various reaction stages by setting the reaction time to 1 h (a,b,c), 2 h (d,e,f), 4 h (h,i,j), 8 h (k,l,m), respectively.

To understand the formation mechanism of 3D hierarchical $NiCo_2O_4$ nanoneedle arrays on Ni foam, time-dependent experiments were carried out. The corresponding

SEM images of the evolution process are shown in **Fig. 2**. At the initial reaction for 1 h, thin and dense layer of nanosheets are uniformly formed on the surface of the Ni foam (**Fig. 2a, 2c**), the structure which also can be clearly observed from the side view (**Fig. 2b**). After the reaction for 2h, the thickness of the nanosheets became thicker, especially at the bottom of the walls. (**Fig. 2d, 2e, 2f**) When the reaction time was extened to 4 h, some tiny nanoneedles with length of about 1 μm appear on the surface of the nanosheets. (**Fig. 2h, 2i, 2j**) Further increasing the reaction time to 8 h, the nanoneedles rooted in the nanosheets became longer and denser, resulting in a coverage of nanoneedles on the surface, as in **Fig. 2k, 2m**. Obviously, side view reveals that the nanoneedles are long and slim (**Fig. 2l**). The morphology transformation from nanosheets into nanosheets-nanoneedles is attributed to $NH_4F$, which not only promotes nanoneedles rooting in nanosheets, but also enhances adhension between the substrate and the arrays.[13, 32, 39] Subsequently, the nanoneedles fully fill the intervals between the primary nanosheets and continue to grow longer and denser with increasing reaction time.

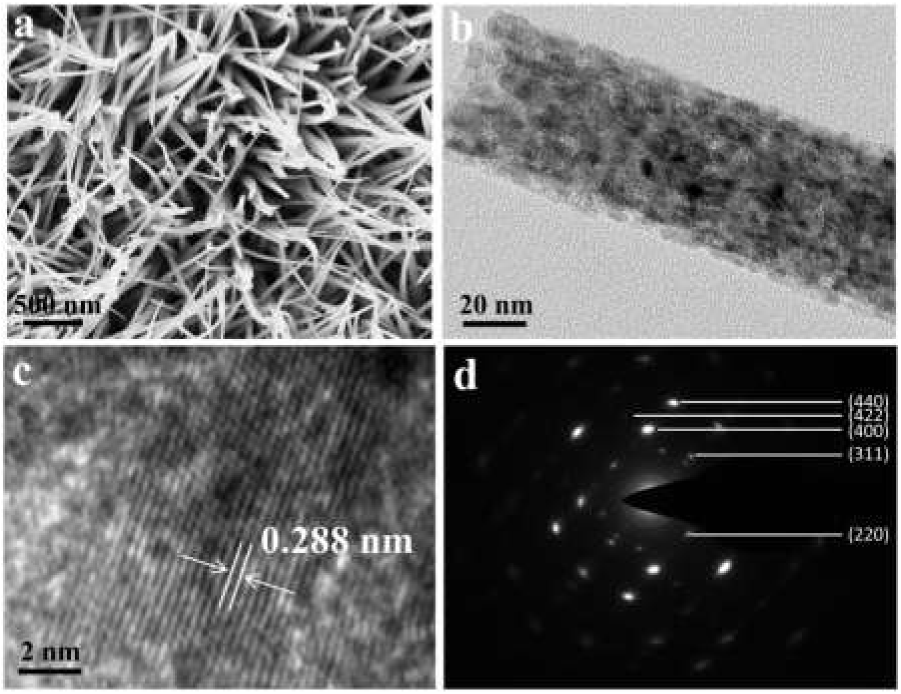

**Fig. 3.** (a) SEM images of $NiCo_2O_4$ nanoneedles grow on Ni foam. (b) TEM image and (c) high-magnification TEM image of a $NiCo_2O_4$ nanoneedle. (d) Diffraction pattern of a $NiCo_2O_4$ nanoneedle.

To further character the structure of $NiCo_2O_4$ nanoneedles, we carried out TEM studies. The TEM image shows that the $NiCo_2O_4$ nanoneedles are highly porous. (**Fig. 3b**) The HRTEM image presented in **Fig. 3c** shows the lattice spacing of 0.288 nm corresponds to the (220) crystal plane of spinel $NiCo_2O_4$. The selected area of electron diffraction (SAED) pattern shows that the porous $NiCo_2O_4$ nanoneedles are polycrystalline (**Fig. 3d**). The diffraction rings and spots in SAED can be indexed by the spinel $NiCo_2O_4$ crystal structure (JCPDS No.73-1702).

To evaluate the properties of the obtained different $NiCo_2O_4$ arrays on Ni foam as the electrode for supercapacitors, electrochemical measurements were then performed. **Fig. S6** shows the CV analysis measured at various scan rates with a potential window from 0 to 0.75 V versus Hg/HgO. All the CV curves present a pair of well-defined redox peaks, indicating the faradic redox reactions related to

M-O/M-O-OH (M refers to Ni or Co) associated with $OH^-$ anions.[40-42] Increasing the scanning rate, the redox current increased, meanwhile, the anodic/cathodic peak shifted in the reverse positive/negative potential, respectively.

## Electrochemical measurement

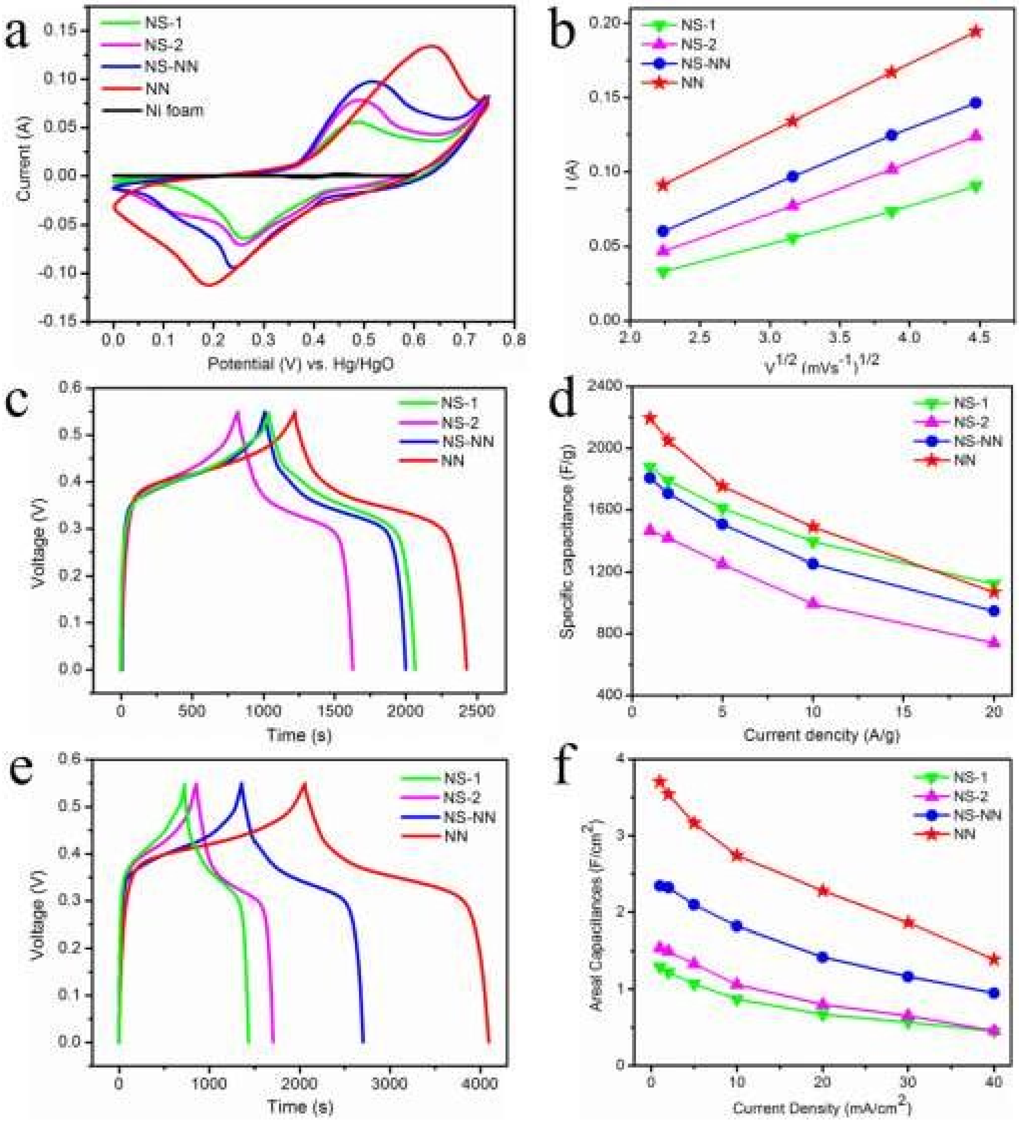

**Fig. 4.** (a) CV curves of $NiCo_2O_4$ nanosheets-1h (NS-1), nanosheets-2h (NS-2), nanosheets-nanoneedles-4h (NS-NN), nanoneedles-8h (NN) arrays, and Ni foam at a scan rate of 10 mV/s, respectively. (b) Dependence of the current density on $v^{1/2}$ for the $NiCo_2O_4$/Ni foam electrodes. (c) and (e) Charge and discharge curves of NS-1, NS-2, NS-NN, and NN at a current density of 1 A/g and 1 $mA/cm^2$, respectively. (d) and (f) Specific capacitances and areal capacitances of the electrodes as a function of current density, respectively.

In order to clearly illustrate the morphology superiority, the electrochemical properties of the $NiCo_2O_4$ array electrodes are further evaluated under the same conditions. The CV curves presented in **Fig. 4a** demonstrate that the $NiCo_2O_4$ nanoneedle arrays on Ni foam showed the strongest peak and biggest area suggesting the highest electrochemical reaction activity. The exact reason for the different electrochemical performances of the $NiCo_2O_4$ array electrodes may be attributed to differences in electrode polarization behavior during the individual electronic transition of $Co^{2+}$, $Co^{3+}$, $Ni^{2+}$ and $Ni^{3+}$ or the combined effect of transition states of $Co^{2+}/Co^{3+}$ and $Ni^{2+}/Ni^{3+}$, which is related to the physical morphology of electrode material.[43, 44] The relationship of the electrochemical capacitances of the $NiCo_2O_4$ arrays can be proved by the plot of anodic peak current with the square root of scanning potential, shown in **Fig. 4b**. The linear responses of the graphs suggest that the redox process is diffusion controlled, and a steeper slope generally means faster protons diffusion. In the alkaline electrolyte, the redox reactions are expressed as follows,[31]

$$\mathrm{NiCo_2O_4} + \mathrm{OH^-} + \mathrm{H_2O} \leftrightarrow \mathrm{NiOOH} + 2\mathrm{CoOOH} + \mathrm{e^-} \quad (10)$$

$$\mathrm{CoOOH} + \mathrm{OH^-} \leftrightarrow \mathrm{CoO_2} + \mathrm{H_2O} + \mathrm{e^-} \quad (11)$$

To get more information about the performance of the as-synthesized $NiCo_2O_4$ array electrodes, galvanostatic charge–discharge measurements were further performed. From **Fig. 4c** and **4e**, it can be seen that both charge and discharge times of the hierarchical $NiCo_2O_4$ nanoneedle structure are much longer than that of $NiCo_2O_4$ nanosheets and nanosheet-nanoneedle arrays, in excellent agreement with

CV results shown in **Fig. 4a**. This is because the high active mass loading results in increased electrode thickness of nanosheets-2h than nanosheets-1h. (**Fig. 2**) The diffusion distance of electrolytes into pseudocapacitor is only in the few nanometers from the surface. Resultingly, thicker electrode leads to the appearance of more “dead” or “inactive”, which cannot participate in the Faradaic reactions.[34, 45] Therefore, the specific capacitance of nanosheets-2h is smaller than that of nanosheets-1h. Further increasing the reaction time, some tiny short nanoneedles appear on the surface of the nanosheets and the nanosheets became longer and denser as the elongation of the reaction time. The additionally long and slim nanoneedles make the specific capacitance of the as-prepared $NiCo_2O_4$ electrode increased. Importantly, a smaller IR drop for the hierarchical $NiCo_2O_4$ nanoneedle structure is found at the beginning of the discharge curve, demonstrating a lower internal resistance of this morphology. It is worth noting that the discharge areal capacitances, calculated by equation (1) at 1 mA/cm$^2$, are increasing as the morphology evolution. **(Fig. 4e)** The areal capacitances turn out to be 1.30, 1.54, 2.34 and 3.71 F/cm$^2$ for nanosheets-1h, nanosheets-2h, nanosheets-nanoneedles-4h, and nanoneedles-8h arrays, respectively. However, the specific capacitance of nanosheets-1h is calculated to be 1878 F/g at 1 A/g, lower than that of nanoneedles-8h for 2193 F/g but higher than that of nanosheets-2h and nanosheets-nanoneedles-4h for 1464 F/g and 1806 F/g, respectively. **(Fig. 4c)** The CV curve of Ni foam compared to that of other four $NiCo_2O_4$ structures are shown in **Fig. 4a**, which demonstrates that the Ni foam contributes little to the total capacitance of the electrode. Therefore, the effect of Ni foam for the capacitance can be ignored.

**Fig. 4d** and **4f** show the electrochemical capacitances of the $NiCo_2O_4$ arrays at various discharge current densities for comparison. As expected, the nanoneedle arrays have the highest specific capacitance and areal capacitance. Even under a current density of 20 A/g, the nanoneedle electrode still has a specific capacitance of 1069 F/g. It also exhibits high areal capacitances of 3.71 F/cm$^2$ at 1 mA/cm$^2$ and 1.39 F/cm$^2$ at 40 mA/cm$^2$. The reason is that the ions in the electrolyte are believed to diffuse almost fully into the holes of the electrode at low scan rate, while a lower capacitance is observed at high scan rate because of the seriously reduced contact between the ions and the electrode. Compared with other reported specific capacitance and areal capacitance of $NiCo_2O_4$ nanostructures or even core/shell hybrid structures, the capacitance values of the hierarchical $NiCo_2O_4$ nanoneedle arrays are superior. (see **Table S1**) The above results demonstrate that the 3D hierarchical nanoneedle structure of the pseudocapacitive materials could enhance capacitance.

As shown in **Fig. S7** and **Fig. S8**, the shapes of the constant current charge-discharge curves at different current density are very similar and hold excellent capacitive behavior. Encouragingly, the $NiCo_2O_4$ nanoneedle arrays electrode exhibits outstanding performance of rate capability. The areal capacitances are 3.71, 3.54, 3.17, 2.74 and 2.28 F/cm$^2$ at current densities of 1, 2, 5, 10 and 20 mA/cm$^2$, respectively. The specific capacitances are 2193, 2048, 1753 and 1490 F/g at current densities of 1, 2, 5 and 10 A/g, respectively.

A good electrochemical supercapacitor should possess a high energy density at high current density. **Fig. S9** shows the Ragone plots of the energy densities and the power densities calculated by equation (2) and (3), respectively. With increasing power density, all the energy densities decrease slowly, and the $NiCo_2O_4$ nanoneedle electrode exhibits highest energy density and highest power density simultaneously. It reaches 92.1 Wh/kg at a power density of 275 W/kg, and still remains 44.9 Wh/kg at a power density of 5500 W/kg. These values are superior to other reported for $NiCo_2O_4$-based supercapacitors,[33, 46] demonstrating that the hierarchical $NiCo_2O_4$ nanoneedle structure is a great potential electrode material in supercapacitors.

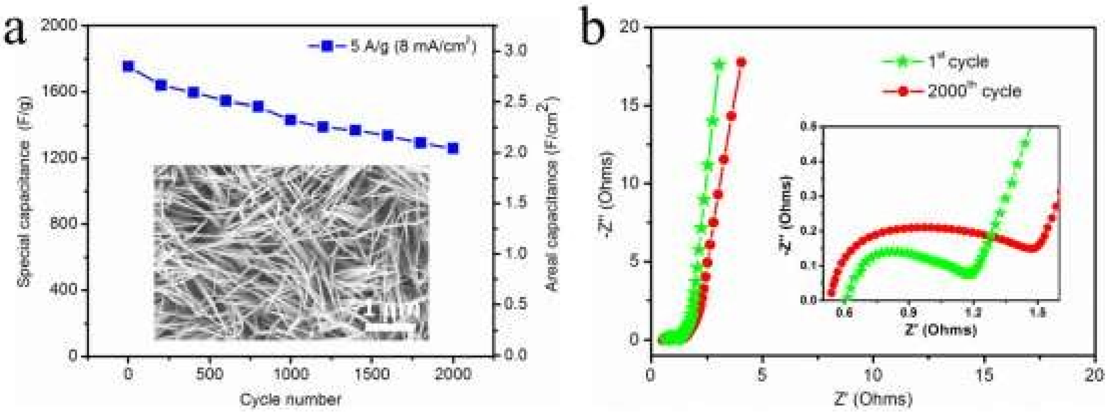

**Fig. 5.** Electrochemical characterization of the hierarchical $NiCo_2O_4$ nanoneedle arrays electrode: (a) Cycling performance, (b) Nyquist curve of the 1st and 2000th cycle of the electrode. The insets are an enlarged curve of the high frequency region and the equivalent circuit.

Since the hierarchical $NiCo_2O_4$ nanoneedle arrays have the highest areal capacitance, specific capacitance and fastest protons diffusion, more electrochemical properties of this structure are explored. The long cycle life was investigated at a current density of 5 A/g (8 mA/$cm^2$) for 2000 cycles. (**Fig. 5a**) Impressively, the specific capacitance of the $NiCo_2O_4$ nanoneedle arrays electrode is still 1260 F/g

(2.06 F/cm$^2$) with 72% retention. The SEM images of $NiCo_2O_4$ nanoneedle arrays after 2000 cycles are shown in **Fig. S10**. It is interested to find that the morphology of nanoneedles keeps well except slightly aggregates. Owing to the constraint of crosslinked nanosheets at the bottom, the nanoneedles on the top would not aggregate seriously. The advantages of this 3D hierarchical nanoneedle structure are further confirmed.

The corresponding EIS of the electrode at the initial stage and after 2000 cycles were further carried out and shown in **Fig. 5b**. Both the impedance spectra display a similar form with a semicircle in the high-frequency region and present a linear region over the low-frequency range. The linear region corresponds to the Warburg impedance ($Z_w$), which represents the electrolyte diffusion to the electrode surface. The slops of the low-frequency straight line of the electrode after 1 and 2000 cycles are almost similar. In the high-frequency region, the intersections at the real part ($Z'$) indicates the solution resistance ($R_s$), and the semicircle corresponds to the charge transfer impendence ($R_{ct}$) in the electrochemical process. As can be seen from the inset, although the $R_s$ after 2000th cycle is slightly bigger than that of the 1st cycle, the ($R_{ct}$) increase is relatively obvious after 2000 cycles, leading to a capacity fading during the cycling process.

Multiple contributing factors can be considered for the high capacitance, good rate capability and long cycle life of the binder-free $NiCo_2O_4$ nanoneedle arrays. First, the $NiCo_2O_4$ materials with a high active mass loading adhered directly on Ni foam substrate can enhance the stability of the electrode material and increase the electrical conductivity of the electrode. Second, the 3D hierarchical nanoneedle arrays morphology is advantageous in ion and electron transport due to the shorter transport path of the nanowire comparing to other structures. Third, the hierarchical array with bottom crosslinked nanosheets possesses a favorable morphological and phase stability because it can release stress caused by volume expansion and redox reactions during electrochemical reaction. Therefore, these structural features will undoubtedly bring about the superior electrochemical performance of the 3D hierarchical nanoneedle arrays over the other $NiCo_2O_4$ structure electrodes.

## Conclusion

In conclusion, we have prepared 3D hierarchical $NiCo_2O_4$ nanoneedle arrays on nickel foam through a facile hydrothermal method followed by annealing in air. Our results demonstrate that the $NiCo_2O_4$ morphology can be simply controlled by prolonging reaction time, and the nanoneedle arrays electrode exhibits the highest specific and areal capacitance. This difference in electrochemical performances is attributed to the high active mass loading and the unique properties of the 3D hierarchical $NiCo_2O_4$ nanoneedle structure with bottom crosslinked nanosheets, which provide various electro active sites for fast redox reaction, shorten the diffusion pathway for ion and electron transport and better accommodate the volume expansion. It is believed that the unique 3D hierarchical array electrode would hold a great promise for high-performance supercapacitors and other energy-storage devices.

## Acknowledgments

We thank the National High Technology Research and Development Program of China (863Program) (2013AA050905), the National Natural Science Foundation of China (No.51222212), the financial support of LPMT, CAEP (ZZ13007 and ZZ14004), Project 2013A030214 supported by CAEP, the Science and Technology Foundation of China Academy of Engineering Physics (No. 2012B0302041) for their financial support. We are grateful to Margaret Yau, Xichuan Liu and Hui Zhang for their valuable discussions and assistance in measurements.

## References

1. S. P. Jiang, *J. Mater. Sci.*, 2008, **43**, 6799-6833.

2. H. S. Liu, C. J. Song, L. Zhang, J. J. Zhang, H. J. Wang and D. P. Wilkinson, *J. Power Sources*, 2006, **155**, 95-110.

3. M. Beidaghi and Y. Gogotsi, *Energy Environ. Sci.*, 2014, **7**, 867-884.

4. G. P. Wang, L. Zhang and J. J. Zhang, *Chem. Soc. Rev.*, 2012, **41**, 797-828.

5. V. Chabot, D. Higgins, A. P. Yu, X. C. Xiao, Z. W. Chen and J. J. Zhang, *Energy Environ. Sci.*, 2014, **7**, 1564-1596.

6. A. Kraytsberg and Y. Ein-Eli, *Adv. Energy Mater.*, 2012, **2**, 922-939.

7. R. V. Noorden, Nature, 2014, 507, 26-28.

8. J. R. Miller and P. Simon, *Science*, 2008, **321**, 651-652.

9. C. Guan, J. P. Liu, C. W. Cheng, H. X. Li, X. L. Li, W. W. Zhou, H. Zhang and H. J. Fan, *Energy Environ. Sci.*, 2011, **4**, 4496-4499.

10. J. P. Cheng, J. Zhang and F. Liu, *RSC Adv.*, 2014, **4**, 38893-38917.

11. P. H. Yang, Y. Ding, Z. Y. Lin, Z. W. Chen, Y. Z. Li, P. F. Qiang, M. Ebrahimi, W. J. Mai, C. P. Wong and Z. L. Wang, *Nano Lett.*, 2014, **14**, 731-736.

12. X. Peng, L. L. Peng, C. Wu and Y. Xie, *Chem. Soc. Rev.*, 2014, **43**, 3303-3323.

13. X. H. Xia, Y. Q. Zhang, D. L. Chao, C. Guan, Y. J. Zhang, L. Li, X. Ge, I. M. Bacho, J. P. Tu and H. J. Fan, *Nanoscale*, 2014, **6**, 5008-5048.

14. R. B. Rakhi, W. Chen, D. K. Cha and H. N. Alshareef, *Nano Lett.*, 2012, **12**, 2559-2567.

15. Y. J. Sun, X. P. Xiao, P. J. Ni, Y. Shi, H. C. Dai, J. T. Hu, Y. L. Wang, Z. Li and Z. Li, *Electrochim. Acta*, 2014, **121**, 270-277.

16. L. Yu, G. Q. Zhang, C. Z. Yuan and X. W. Lou, *Chem. Commun.*, 2013, **49**, 137-139.

17. C. C. Hu, K. H. Chang, M. C. Lin and Y. T. Wu, *Nano Lett.*, 2006, **6**, 2690-2695.

18. T. Y. Wei, C. H. Chen, H. C. Chien, S. Y. Lu and C. C. Hu, *Adv. Mater.*, 2010, **22**, 347-351.

19. J. W. Xiao and S. H. Yang, *RSC Adv.*, 2011, **1**, 588-595.

20. N. Padmanathan and S. Selladurai, *RSC Adv.*, 2014, **4**, 8341-8349.

21. Y. Q. Wu, X. Y. Chen, P. T. Ji and Q. Q. Zhou, *Electrochim. Acta*, 2011, **56**,

7517-7522.

22. L. Qian, L. Gu, L. Yang, H. Y. Yuan and D. Xiao, *Nanoscale*, 2013, **5**, 7388-7396.

23. Y. Lei, J. Li, Y. Y. Wang, L. Gu, Y. F. Chang, H. Y. Yuan and D. Xiao, *ACS Appl. Mater. Interfaces*, 2014, **6**, 1773-1780.

24. G. Q. Zhang, H. B. Wu, H. E. Hoster, M. B. Chan-Park and X. W. Lou, *Energy Environ. Sci.*, 2012, **5**, 9453-9456.

25. W. W. Zhou, D. Z. Kong, X. T. Jia, C. Y. Ding, C. W. Cheng and G. W. Wen, *J. Mater. Chem. A*, 2014, **2**, 6310-6315.

26. Z. Y. Wang, Y. F. Zhang, Y. H. Li and H.Y. Fu, *RSC Adv.*, 2014, **4**, 20234-20238.

27. Z.-Q. Shi, L.-X. Jiao, J. Sun, Z.-B. Chen, Y.-Z. Chen, X.-H. Zhu, J.-H. Zhou, X.-C. Zhou, X.-Z. Li and R. Li, *RSC Adv.*, 2014, **4**, 47-53.

28. G. Q. Zhang and X. W. Lou, *Sci. Rep.*, 2013, **3**, 1470-1475.

29. P. Meduri, E. Clark, J. H. Kim, E. Dayalan, G. U. Sumanasekera and M. K. Sunkara, *Nano Lett.*, 2012, **12**, 1784-1788.

30. J. Jiang, Y. Y. Li, J. P. Liu, X. T. Huang, C. Z. Yuan and X. W. Lou, *Adv. Mater.*, 2012, **24**, 5166-5180.

31. C. Z. Yuan, J. Y. Li, L. R. Hou, X. G. Zhang, L. F. Shen and X. W. Lou, *Adv. Funct. Mater.*, 2012, **22**, 4592-4597.

32. Y. J. Chen, B. H. Qu, L. L. Hu, Z. Xu, Q. H. Li and T. H. Wang, *Nanoscale*, 2013, **5**, 9812-9820.

33. W. W. Liu, C. X. Lu, K. Liang and B. K. Tay, *J. Mater. Chem. A*, 2014, **2**, 5100-5107.

34. D. P. Cai, B. Liu, D. D. Wang, L. L. Wang, Y. Liu, H. Li, Y. R. Wang, Q. H. Li and T. H. Wang, *J. Mater. Chem. A*, 2014, **2**, 4954-4960.

35. H. W. Wang and X. F. Wang, *ACS Appl. Mater. Interfaces*, 2013, **5**, 6255-6260.

36. X. H. Xia, J. P. Tu, Y. Q. Zhang, X. L. Wang, C. D. Gu, X. B. Zhao and H. J. Fan, *ACS Nano*, 2012, **6**, 5531-5538.

37. J. W. Ward, *J. Catal.*, 1968, **10**, 34-46.

38. J. F. Marco, J. R. Gancedo, M. Gracia, J. L. Gautier, E. I. Rios, H. M. Palmer, C. Greaves and F. J. Berry, *J. Mater. Chem.*, 2001, **11**, 3087-3093.

39. Q. Yang, Z. Y. Lu, J. F. Liu, X. D. Lei, Z. Chang, L. Luo and X. M. Sun, *Prog. Nat. Sci*, 2013, **23**, 351-366.

40. L. Huang, D. C. Chen, Y. Ding, S. Feng, Z. L. Wang and M. L. Liu, *Nano Lett.*, 2013, **13**, 3135-3139.

41. X. Y. Liu, S. J. Shi, Q. Q. Xiong, L. Li, Y. J. Zhang, H. Tang, C. D. Gu, X. L. Wang and J. P. Tu, *ACS Appl. Mater. Interfaces*, 2013, **5**, 8790-8795.

42. G. H. Zhang, T. H. Wang, X. Z. Yu, H. N. Zhang, H. G. Duan and B. G. Lu, *Nano Energy*, 2013, **2**, 586-594.

43. Q. F. Wang, X. F. Wang, B. Liu, G. Yu, X. J. Hou, D. Chen and G. Z. Shen, *J. Mater. Chem. A*, 2013, **1**, 2468-2473.

44. Y. G. Li, P. Hasin and Y. Y. Wu, *Adv. Mater.*, 2010, **22**, 1926-1929.

45. P. Simon and Y. Gogotsi, *Nat. Mater.*, 2008, **7**, 845-854.

46. X. Y. Liu, Y. Q. Zhang, X. H. Xia, S. J. Shi, Y. Lu, X. L. Wang, C. D. Gu and J. P. Tu, *J. Power Sources*, 2013, **239**, 157-163.

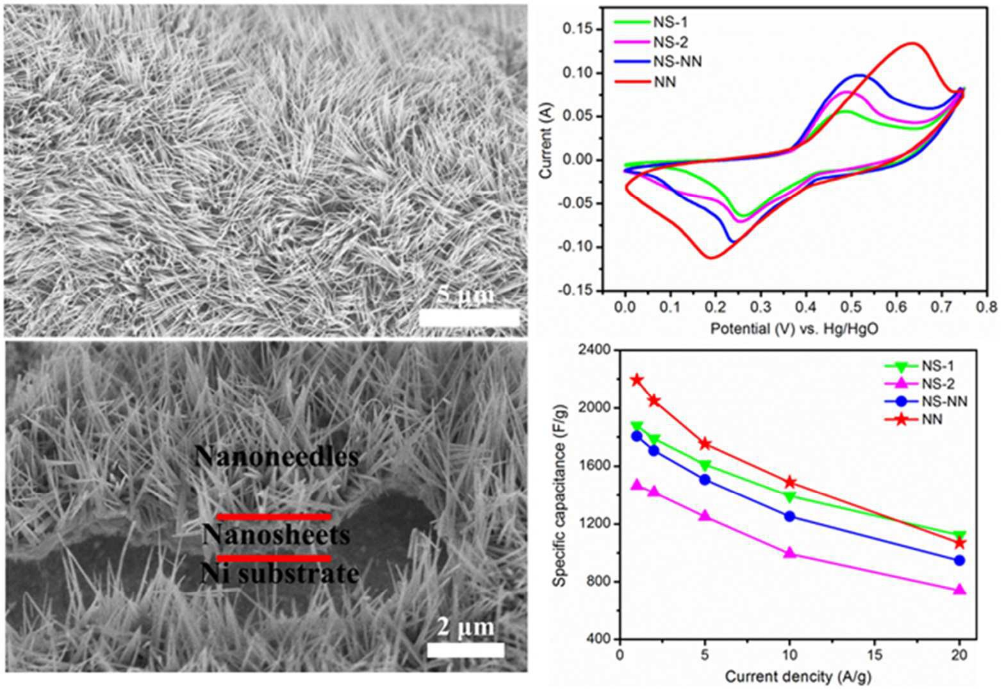

A novel NiCo2O4 nanoneedle arrays with bottom crosslinked nanosheets grew on Ni foam as advanced binder-free electrodes via a facile one-step hydrothermal method followed by annealing in air, which exhibited high electrochemical performance.
57x39mm (300 x 300 DPI)